



Highly efficient and rapid manufactured perovskite solar cells via Flash InfraRed Annealing

Sandy Sánchez^{1,2,*}, José Jerónimo-Rendon^{1,3}, Michael Saliba^{3,4}, Anders Hagfeldt^{2,*}

¹ Adolphe Merkle Institute, University of Fribourg, Chemin des Verdiers 4, 1700 Fribourg, Switzerland

² Laboratory of Photomolecular Science (LSPM), École Polytechnique Fédérale de Lausanne (EPFL), 1015 Lausanne, Switzerland

³ Institute of Materials Science, TU Darmstadt, Alarich-Weiss-Strasse 2, 64287 Darmstadt, Germany

⁴ Helmholtz Young Investigator Group, IEK5-Photovoltaik, Forschungszentrum Jülich, 52425 Jülich, Germany

This work unveils how to quickly manufacture highly efficient and stable perovskite solar cells (PSCs) using the Flash InfraRed Annealing (FIRA) method. With FIRA, the titanium oxide mesoscopic layer can be synthesized in only 10 min, and the synthesis of the perovskite film takes a few seconds. All is done in one place and continuously, allowing a better synchronization of the manufacturing process with high reproducibility. For this purpose, a new perovskite composition based on formamidinium (FA) lead iodide combined with a passivation post-treatment has been optimized, improving the film quality for PSCs. Here we show a step forward into the industrial application of the FIRA method in PSCs.

Introduction

Renewable energies are essential for reducing the greenhouse effect across the earth. Global carbon emissions have significantly increased as the cost of PV technologies falls and their working efficiency continues to rise [1–3]. In this context, the recent development of perovskite solar cells (PSCs) has demonstrated a technological revolution in the field of semiconductor devices [4–6]. New architectures, processes and deposition methods are improving the stability and the power conversion efficiency (PCE) of such solar cells [7–13]. However, a great deal of effort is needed to commercialize this technology, and the FIRA (Flash InfraRed Annealing) method that allows the rapid manufacture of PSCs can be one solution for large-scale manufacturing processing and market requirements [14–20].

Following the recent works on FIRA, now for the first time, we are able to synthesize in 10 min the TiO₂ mesoscopic layer using the FIRA installation, achieving in addition with the FIRA manufacturing processing of PSCs over 20% of PCE. This is significant in terms of environmental impact taking into account the low

energy consumption compared to the conventional use of an annealing step at 450 °C to sinter the TiO₂ film [20,21]. Consequently, the manufacturing device time can also be reduced, which allows better synchronization with the whole procedure and can compete in terms of shorter time with those reported in the literature [22–25]. Together with the perovskite synthesis, made in only 1.6 s, we simplified the procedure to develop FIRA as a single installation to manufacture PSCs in less than 1 h.

In this work a new perovskite formulation adapted to the FIRA crystallization requirement has been developed, enabling us to manufacture highly efficient and stable PSCs. The used perovskite solution is based on formamidinium (FA) lead iodide with the addition of small amounts of cesium (Cs) and guanidinium (GA). Indeed, it is methylammonium-free, ensuring better thermal stability and longer FIRA annealing time, which allows the preparation of highly crystalline perovskite films [26–30]. The cation composition is based on FA (80%), Cs (15%) and guanidinium, GA (5%). We denote this composition in the following FCG. This composition is able to stabilize the black perovskite phase and to make compact films throughout the FIRA synthesis. Following this, we compare the standard procedure called antisolvent (AS) and the more stabilised triple cation perovskite solution, containing methylammonium (MA)

* Corresponding authors.

E-mail addresses: Sánchez, S. (sandy.sanchezalonso@epfl.ch), Hagfeldt, A. (anders.hagfeldt@epfl.ch).

bromide and cesium iodide, with the FCG perovskite proceed by FIRA [68]. We denote the devices made with the AS procedure and triple cation standard perovskite as Mix-AS. Recently, in the literature, we can find numerous successful applications based on FA lead iodide perovskite [26,31–34], but to date, this specific stoichiometry adapted for FIRA is novel.

Regarding the advantages of GA cation integration in perovskites compositions, Jodlowski et al. proved that this addition to MA exhibits superior photovoltaic performance and material stability compared with single cation MAPbI₃ [35]. On the other hand, Pham et al., pointed out that a post-treatment of GA thiocyanate induces large crystal domains, facilitating improved cell stability and high performance [36]. De Marco et al., demonstrated a passivation effect through GA-based additives to achieve extraordinarily enhanced carrier lifetimes and higher open circuit voltages [37].

As known in the literature, the FAPbI₃ composition display a polymorphism between δ and α phases at room temperature, and one of the solutions to stabilize the black phase is to have a mix cation composition with, for example, the addition of the MA molecule [38–44]. Here, we perform a mix perovskite composition with large GA and Cs cations to improve its stability. Still, this is not enough to keep the black phase stable for long-term [45–47]. Therefore, a post-treatment with tetrabutylammonium iodide (TBAI) is performed, which improves the film quality and the stability of the perovskite α -phase. The treatment suggests a passivation pathway, which improves the charge injection in the hole transport material (HTM) and removes defect at the grain boundaries of the perovskite film. These improvements combined with the FIRA method make it possible to obtain highly efficient large-area devices, with a PCE for an area of 1.4 cm² up to 17%. Our results are thus a step forward to cost-efficient large-scale manufacturing of PSCs [20].

Rapid annealed TiO₂ mesoscopic film

Rapid thermal annealing through FIRA was applied to the TiO₂ mesoscopic layer, as mentioned in the introduction. Fig. 1a shows the temperature profile of the FIRA as a function of time, consisting of 10 cycles of 15 s FIRA-on, plus 45 s of FIRA-off. The consumed time was 10 min for the sintering of one batch (150 cm² of total area can be annealed in one time), plus 10 min more with similar annealing procedure for the lithium treatment (see Experimental section). The maximum recorded temperature was 640 °C and the median roughly 620 °C. The highest temperature was kept for only a few seconds. It went down quickly due to the water cooling system and gas flow. Note that this temperature was measured on the sample holder in the chamber, which is constantly under cooling.

Fig. 1b shows the X-ray pattern of a TiO₂ film annealed by our regular procedure, i.e. on a hotplate at 450 °C during 30 min (the whole annealing time lasts 3 h) and a TiO₂ film annealed by the FIRA cycles. As a blank reference we show a FTO substrate, for which the peak at 2 θ 25° is representative of the anatase phase [48–50]. A visual comparison of the annealed TiO₂ from SEM cross-sectional images can be seen in Fig. 1c, showing two electrodes with perovskite films made by FIRA and AS methods, respectively. There are no visible differences in the images, both show a TiO₂ layer with roughly 200 nm and a perovskite with

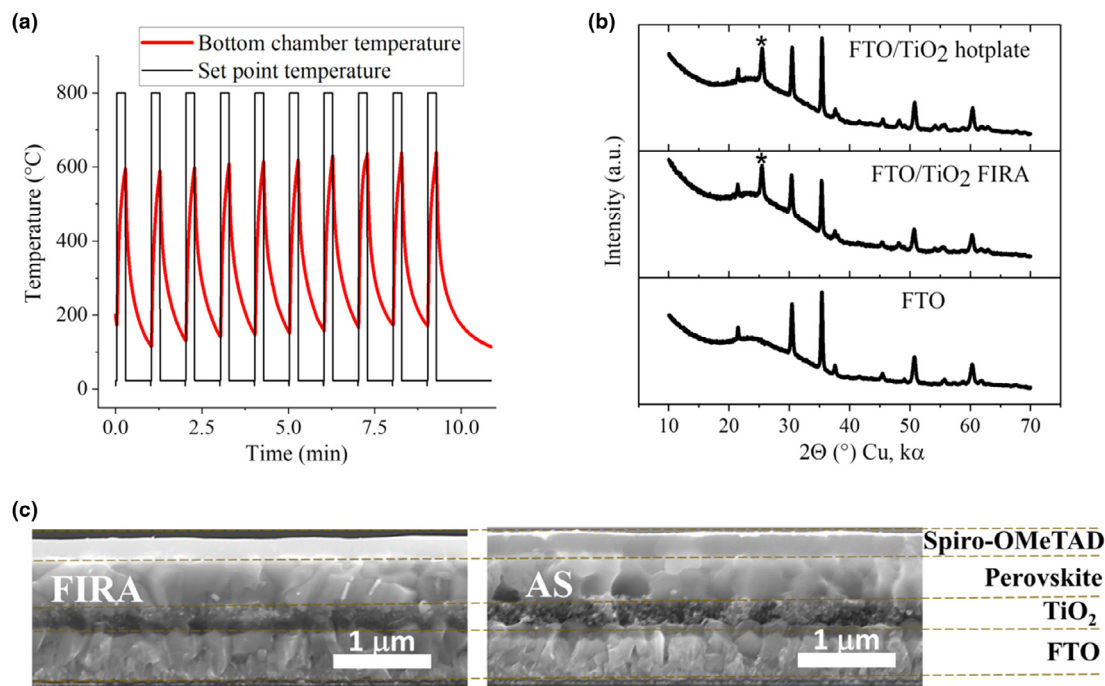
500 nm thickness. The FIRA and conventional (hotplate) annealing results in a similar morphological structure as observed from the cross-sectional images of both devices.

FCG perovskite stabilized with TBAI

After spin-coating the perovskite solution in the electrodes, the films were annealed during 1,6 s of pulse time and kept in the FIRA chamber for an additional 10 s (see Materials and methods section). Fig. 2a shows the X-ray pattern for FA based perovskite compositions, with cation stoichiometry variations. The patterns do not show a significant difference, and the α black phase in the desired three-dimensional cubic system matches all of them, being similar to the results reported by Han et al. for FAPbI₃ single crystal [51]. A small difference is, however, observed in the patterns, i.e., for peaks at 2- θ 22° and 34°, which can be due to different cation stoichiometries. Therefore, there is no evidence of the yellow δ phase [34,38,40,52]. In Fig. S1 is provided a comparison between the α black phase from FIRA annealed samples with tetragonal MAPbI₃ and hexagonal FAPbI₃ crystal systems. The similarity in peak position and intensity suggests that the additional Cs and GA cations can be integrated into the lattice with the FIRA method [53–55]. The chosen annealing time is set to 1.6 s, giving the purest FA-based lead iodide perovskite phase. At this FIRA time there is no evidence of a 2- θ peak at 12°, which is attributed to the remaining PbI₂ phase, as shown in Fig. S2 [56–58].

In order to verify the film crystallization quality, Fig. 2b shows SEM top view images of the related pattern perovskite composition. Here the FA-Cs base perovskite composition does not show a compact film, since gaps can be seen in the grain domain boundary. This can be attributed to the difference in chemical potential of the solutions (before annealing), from the ratios of the cation concentrations, where an excess of cesium can slow down the characteristic FIRA crystal growth, as previously reported [59]. To solve this, the large GA cation was added, which provides extra hydrogen bonding to increase the adhesive molecular force from solution to the substrate, decreasing the surface energy [34,37,60]. Therefore, we are able to grow a bigger grain domain, which collapses at the boundary with other neighborhood grains after FIRA annealing. This results in a compact thin film, as shown in Fig. 2b. The Guanidinium cation addition contributes to planarize the perovskite films under FIRA synthesis, avoiding short circuits due to voids at the grain boundaries (i.e., cesium lead iodide tends to have an island growth mechanism, Fig. 2b). In Fig. S3 the SEM top view images show the gradual GA addition, up to 5% of the total cations, contributing to the compactness of the films and allowing to grow bigger grains domains.

The thermal stability of the FCG perovskite film can also be improved as can be seen in Fig. S4, from a thermogravimetric (comparing different mix compositions) and a calorimetric analysis (comparing different FIRA synthesis times). Regarding the stability of the film and avoiding the phase polymorphism of FAPbI₃ [27,52,61], a post-treatment was included as a second step, with an additional FIRA annealing at low temperature. A few milligrams of TBAI molecule was dissolved in 1 ml of IPA to spin drop after the perovskite deposition. Afterward, the samples were annealed during 15 min at 100 °C in inert atmosphere

**FIGURE 1**

(a) Temperature as a function of time for TiO₂ mesoporous FIRA-annealed films. (b) X-ray pattern for FTO and TiO₂ films. (c) Cross-sectional SEM images of the perovskite solar cell architectures.

(in FIRA furnace mode, see details in Methods). To prove the efficacy of this treatment, two films with FCG perovskite, one with TBAI treatment and the second one without it, were aged in ambient condition, as shown in Fig. 2c – an optical image taken in transmission mode. In Fig. S5 a Zoom-in (50×) of these images can be seen, showing the characteristic internal grain-domain morphology of the FIRA annealed perovskite films.

One month later the FCG composition was degraded as shows the optical image, Fig. 2c top and the respective collected spectrum. Similar to the image, the optical absorption for the aged sample shows a perovskite phase degradation, it does not absorb in the green-red wavelengths, with respect to the pristine spectrum (estimated from optical transmittance). In contrast, the FCG perovskite with TBAI treatment remains stable and no significant differences can be seen with respect to the optical transmittance spectrum after one month, Fig. 2c bottom. This agrees with the XRD pattern collected for both samples as can be seen in Fig. S6, where the TBAI treated films remains with identical α phase, however the pattern of the film without TBAI shows phase segregation, for example at 12° of the 2 θ peak. Following this study, the TBAI treatment shows an increment of the PV parameters for 20 selected devices (with and without TBAI) as shown Fig. S7. Mainly, the fill factor (FF) and the PCE have an average increment of 10% and 2.3%, respectively, after TBAI. This performance increment can be attributed to the passivation in the perovskite/HTM interface, suppressing recombination losses.

Finally, a PL spectrum was collected for FCG and Mix perovskite to establish the optical gap of both compositions, in relation to its halide stoichiometry, as can be seen in Fig. 2d. Due to the presence of 10% of bromide for the Mix perovskite, the band-

gap is blue shifted with respect to FCG perovskite, containing 100% of iodide [62–64]. The normalized PL intensity for Mix perovskite is slightly lower than the FCG, but this does not represent a significant difference to consider for further analysis and is beyond the scope of this work.

PV performance of the manufactured PSCs

FCG perovskite is used in this work in a regular PSC architecture containing: FTO/TiO₂/Perovskite/Spiro/Au. The PV performances of the three devices with similar architecture but different perovskite compositions and manufacturing methods are studied. FCG perovskite is synthesized by FIRA and AS (both devices use the TiO₂ mesoporous layer made by FIRA-cycles), and the Mix (FA-MA-Cs) composition was made with regular (AS) procedure, which includes the TiO₂ mesoporous layer annealed in a standard hotplate. First, Fig. 3a shows the *JV* curves of the champion PSCs and its respective PV parameters, all of them with PCE over 20% denoting high-performance devices. The hysteresis of the all FIRA FCG processed device is slightly higher than the AS processed perovskite, as observed by the difference in PCE for the forward scan, having a decrease of 5% with respect to the backward initial scan. Fig. 3b shows the IPCE of an all-FIRA synthesized FCG device, showing a high external quantum efficiency and the lowest bandgap energy with respect to the Mix composition, in agreement with Fig. 2d. In the IPCE graph in Fig. 3b, the integrated photocurrent gives a value of 23.8 mA/cm², in good agreement with the *J*_{sc} from the scanned *JV* curve.

Fig. 3c shows the statistics of the PV parameters for 50 manufactured devices of the three chosen sets of PSCs, with its respective manufacturing methods and perovskite composition.

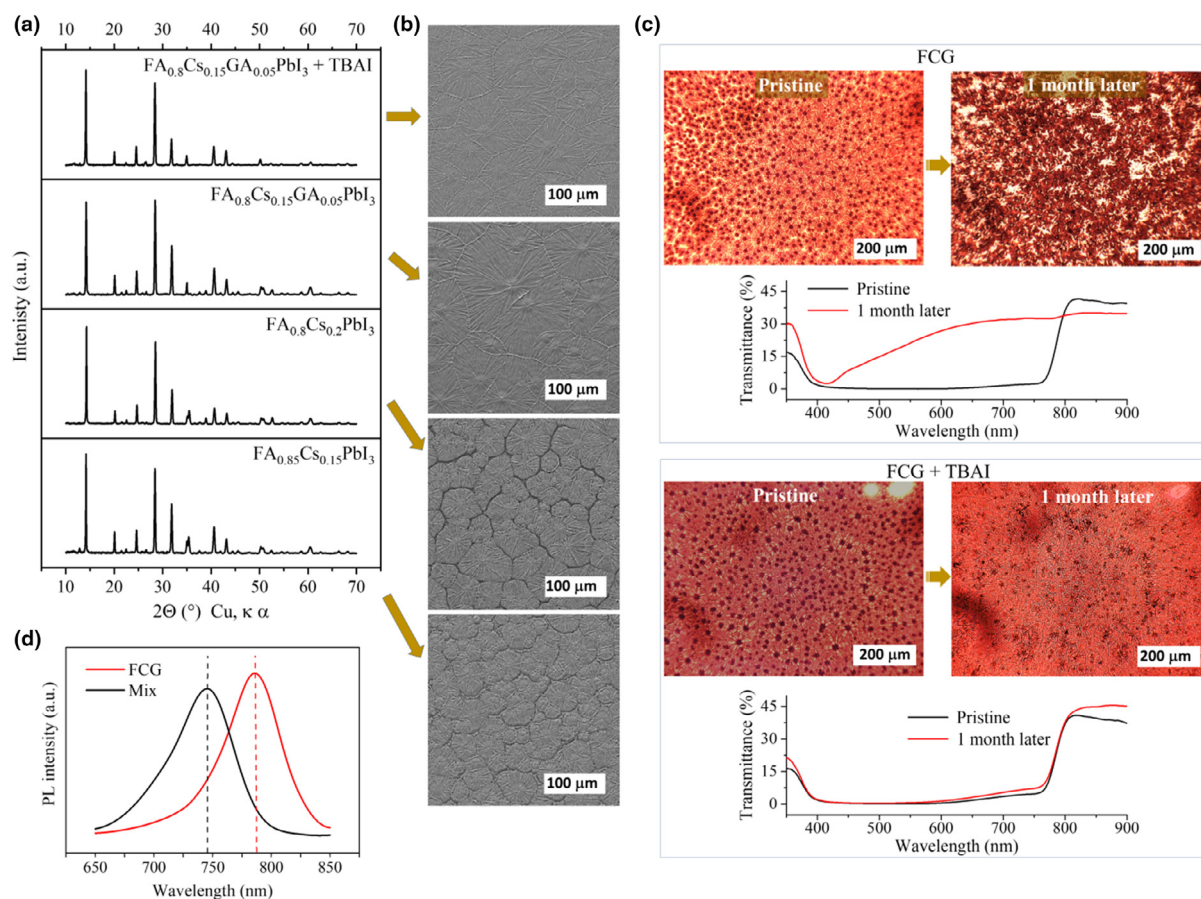


FIGURE 2

Formamidinium base perovskite thin film (a) X-ray pattern, (b) SEM top view images. (c) Optical images taken in transmission mode for FCG perovskite thin film with and without tetrabutylammonium (TBAI) treatment, and optical transmittance spectrum for the chosen image pixels. The films were aged 1 month in ambient conditions, 40% of relative humidity and in shadow. (d) Photoluminescence (PL) spectrum of thin films of the mix and FCG perovskite compositions.

Interestingly, the results show a similar median average value of PCE, being 1% lower for the FCG-all FIRA batch. This is directly related to the slightly lower FF for this batch of PSCs with respect to the AS processed perovskite, which suggests that FIRA processing under ambient conditions (without inert atmosphere) may limit the quality of the perovskite film, as previously reported [14,59]. However, with the FF median average of $69.8 \pm 0.464\%$, there has been an improvement with respect to the previous related works. This can be attributed to the adapted FCG-FIRA perovskite composition and the TBAI treatment, as can be seen in the FF comparison from JV curves for 20 devices (with and without TBAI treatment) in Fig. S8. With respect to the V_{oc} and J_{sc} , the statistics show a good agreement in between the perovskite optical band gap energy and its higher V_{oc} for Mix perovskite and higher J_{sc} for FCG perovskite.

To prove the utility of FIRA-FCG process for larger area devices, Fig. 3d shows the JV curve of a champion device, measured with 1.4 cm^2 of light aperture area. The PCE achieved is up to 17.0% with 16.4% in forward scan, with a median average of $15.9 \pm 0.126\%$ for 30 devices, as shown in supplementary Fig. S9. Finally, Fig. 3e shows the stability measurement for FCG-FIRA and Mix devices with 24% and 20% losses, respectively, after 200 h at 25°C . The Mix-AS shows slightly smaller

decays than the FCG-FIRA device, however, both compositions behave almost similar after the first 50 hours. Once more, the PCE was recorded for both devices 24 h (in dark) after the stability measurement with a recovery of 91.3% (Mix-AS) and 90.7% (FCG-FIRA) respect to the initial efficiencies, as shown in Fig. S10. In both, a reversible decay component can be attributed for the PCE recovery [65–67].

Conclusions

In this work the speed of the manufacturing process has dramatically been improved with respect to previous works, achieving highly efficient and stable PSCs. The TiO_2 mesoscopic layer through FIRA is prepared in only 10 min and yet produces high-quality electrodes for PSCs. The new perovskite composition adapted for FIRA improves the PCE and the stability of the cell in respect to previous rapid thermal annealing works. The preparation of the perovskite layer is made in 1.6 s with the FIRA method. TBAI treatment serves a route to stabilize the FA α phase, which is required for highly stable PSCs, but also contributes to the passivation of the perovskite film improving the quality of the HTM interface. The PV performance of the devices demonstrated that FIRA can be used as a standard method for fast

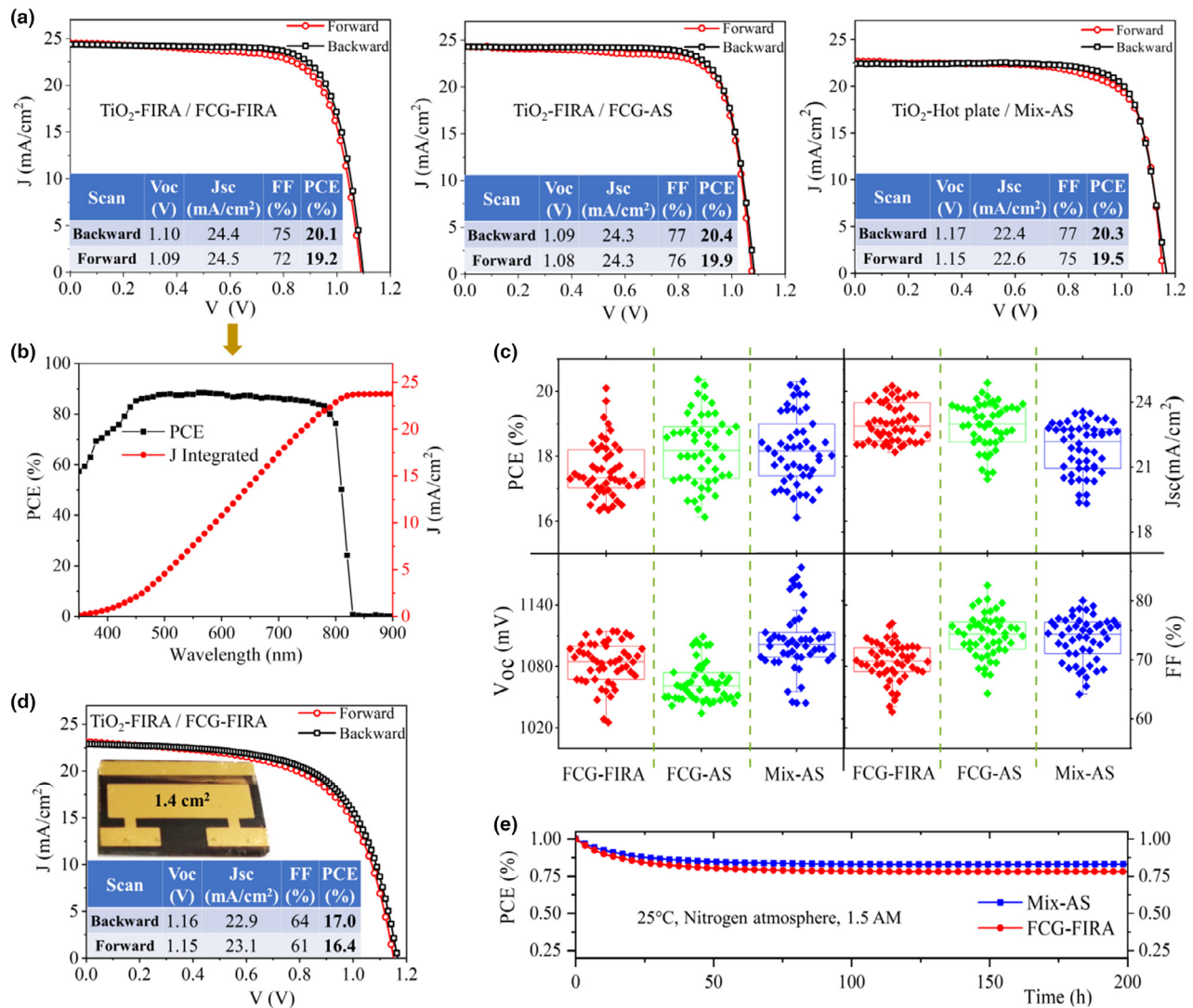


FIGURE 3

(a) *JV* curves, forward and backward scan of the champion devices, scan speed: 10 mV/s and mask aperture area: 0.1 cm². (b) EQE and integrated photocurrent from the FCG labeled champion device. (c) Statistics of the PV parameter for 50 samples of the three studied devices. (d) *JV* curves for the champion large area device with a mask aperture area of 1.4 cm² and scan speed 10 mV/s. (e) Stability measurement recorded at 25 °C in nitrogen atmosphere during 200 h at 1.5 AM, for FCG and Mix labeled devices. The measurements were carried out under constant light and by a *JV* scan each 10 min.

production, high performance and highly reproducibly manufactured devices.

Materials and methods

Device manufacturing

Photovoltaic devices were fabricated on FTO coated glass (Pilkington NSG TEC™). The substrates were cleaned with Hellmanex soap, followed by 30 min sonication in a Hellmanex 2% water solution, 15 min sonication in IPA, and 5 min of oxygen plasma etching. Then, 30 nm thick TiO₂ compact layers were deposited onto the FTO by spray pyrolysis at 450 °C from a precursor solution of titanium diisopropoxide bis (acetylacetonate) in anhydrous ethanol and acetylacetonate. After spraying, the FTO substrates were left at 450 °C for 5 min before cooling to room temperature. A mesoporous TiO₂ layer was deposited by spin-coating for 10 s at 4000 rpm with a ramp of 2000 rpm s⁻¹, using

a 30-nm particle size TiO₂ paste (Dyesol 30 NR-D) diluted in ethanol, 75 mg/ml, to achieve 150–200 nm thick mesoporous layers. After spin-coating, the substrates were annealed by two ways. First and following regular procedure, the FTO substrates were dried at 100 °C for 10 min, and the films were annealed on a programmable hotplate (2000 W, Harry Gestigkeit GmbH) to crystallize TiO₂ at 450 °C for 30 min under dry air flow. The second way was by using the FIRA installation, the substrates were placed on the chamber and annealed under full power mode in dry air during 15 s plus 45 s cooling down, repeated it 10 times.

The Mix hybrid perovskite precursor solution was deposited from a precursor solution containing CH₃N₂I (1 M), PbI₂ (1.1 M), CH₃NH₃Br (0.2 M) and PbBr₂ (0.2 M) in anhydrous DMF:DMSO (from Merck) 4:1 (v:v). Note that this composition contains a lead excess as reported elsewhere [68]. Then CsI, dissolved as a 1.5 M stock solution in DMSO, was added to the

mixed perovskite precursor to achieve the desired triple cation composition. The FCG hybrid perovskite solution was deposited from a precursor solution of $\text{CH}_3\text{N}_2\text{I}$ (1.12 M), PbI_2 (1.4 M), CsI (0.21 M) and GAI (0.07 M) in anhydrous DMF:DMSO 2:1 (v:v). For the tetrabutyl ammonium iodide solution was dissolved 3 mg in 1 ml of Isopropyl alcohol. All the organic salts were acquired in GreatSolar, the lead halides in TCI and DMSO and DMF solvents acquired from Merck.

For the antisolvent method the perovskite films were deposited as previously reported [69,70]. The perovskite solution was spin-coated in two steps at 1000 and 6000 rpm for 10 and 20 s, respectively. During the second step, 100 μL of chlorobenzene was poured onto the spinning substrate, 5 s before the end of the program. The substrates were then annealed at 100 °C for 1 h in a nitrogen-filled glovebox. After perovskite annealing, the substrates were cooled down within a few minutes.

The films made by FIRA method include the spin-coating of the perovskite solution in a single step at 4000 rpm for 10 s. The substrates were then IR irradiated for 1.6 s (for those electrodes used for working devices) in the FIRA oven and were kept there for 10 additional seconds before removal. FIRA processing was carried out in a standard fume hood. A TBAI treatment was carried out by spin coating at 4000 rpm during 20 s the solution on top of perovskite film, then the samples were placed on the FIRA chamber in furnace mode applying 100 °C during 15 min, in an inert atmosphere. Note that two main modes can be used with FIRA, one is full power for fast film synthesis (in order of seconds), and the second in furnace mode, which can be programmed as a standard oven to follow a temperature profile. Immediately after cooling the perovskite films, a spiro-OMeTAD (Merck) solution (70×10^{-3} M in chlorobenzene) was deposited by spin-coating at 4000 rpm for 20 s. Spiro-OMeTAD was doped with Li-TFSI (Sigma Aldrich), tris(2-(1H-pyrazol-1-yl)-4-*tert*-butylpyridine)-cobalt(III) tris(bis(trifluoromethylsulfonyl)imide) (FK209, Dynamo), and 4-*tert*-butylpyridine (TBP, Sigma-Aldrich). The molar ratios of the additives to spiro-OMeTAD were: 0.5, 0.03, and 3.3 for Li-TFSI, FK209, and TBP, respectively.

Photovoltaic device testing

For photovoltaic measurements, a solar simulator from ABET Technologies (Model 11016 Sun 2000) with a xenon arc lamp was used, and the solar cell response was recorded using a Metrohm PGSTAT302N Autolab. The intensity of the solar simulator was calibrated to 100 mW/cm^2 using a silicon reference cell from ReRa Solutions (KG5 filtered). J - V -curves were measured at reverse and forward bias at a scan rate of 10 mV/s ; this slow scan rate was used in all JV measurements to minimize hysteresis effects. A black, non-reflective metal mask with an aperture area of 0.1024 cm^2 was used to cover the active area of the device. In this way the active area of the devices was fixed avoiding artefacts produced by scattered light. IPCE was measured with a commercial apparatus (Arkeo-Ariadne, Cicci Research s.r.l.) based on a 300 W Xenon lamp and able to acquire spectrum from 300 to 1100 nm with 2 nm of resolution. It was recorded as functions of wavelength under a constant white light bias of approximately 5 mW/cm^2 supplied by an array of white light emitting diodes. All measurements were conducted using a non-reflective metal

mask with an aperture area of 0.1024 cm^2 to cover the active area of the device and avoid light scattering through the sides.

The solar cell current transient dynamics (potentiostatic) and the maximum power point tracking data were measured under 1 Sun equivalent white LED illumination using an SP300 biologic potentiostat. Maximum point tracking was done using a home-developed program, which would keep the devices at the maximum power point by creeping oscillation in voltage and which would measure a full J - V curve every 10 min. The devices were placed inside an in-house-developed airtight sample holder, which allowed them to be kept under an inert, nitrogen atmosphere. Additionally, the backside metal electrode of the devices was placed against a Peltier element, which with the use of a PID controller would keep the actual temperature of the device at 25 °C regardless of the illumination or ambient temperature.

Device characterization

Scanning electron microscopy was carried out on a Tescan MIRA 3 LMH with a field emission source operated at an acceleration voltage of 10 kV. Powder X-ray diffraction was performed in transmission geometry with Cu target ($\lambda = 1.5401 \text{ \AA}$) using an STOE STADI P diffractometer. Optical transmission measurements were performed using a Zeiss Axio-Scope A1 Pol using a Zeiss EC Epiplan-Apochromat 10 \times and 50 \times objectives and a xenon light source (Ocean Optics HPX-2000). For spectroscopic measurements, an optical fiber (QP230-2-XSR, 230 μm core) collected the light reflected from the sample. The spectra were recorded by a spectrometer (Ocean Optics Maya2000 Pro), and a standard white diffuser was used as reference. Photoluminescence spectra were obtained with Fluorolog 322 (Horiba Jobin Yvon Ltd) with the range of wavelength from 620 nm to 850 nm by exciting at 460 nm. The samples were mounted at 60° and the emission recorded at 90° from the incident beam path.

The temperature in the FIRA chamber was measured using a K-type thermocouple connected to an Analog Devices AD595 amplifier interfaced with Labview software. Differential Scanning Calorimetry (DSC) measurements were performed using a Mettler-Toledo STAR system under an N_2 atmosphere. Experiments involving different heating and cooling cycles were performed on ~ 3 mg samples placed in standard DSC pans at 10 °C/min. Thermogravimetric analysis for powder materials was carried out in a PerkinElmer TGA 4000. 2–3 mg samples were placed in ceramic pans, and the weight loss was monitored between 25 and 600 °C at a rate of 10 °C/min under a nitrogen flow rate of 20 mL/min. Powder samples were carefully scraped off the substrates right after annealing.

Data availability

Data will be available on request.

Acknowledgement

The project (WASP) leading to this publication, has received funding from the European Union's Horizon 2020 Research and Innovation Programme under grant agreement No 825213.

Appendix A. Supplementary data

Supplementary data to this article can be found online at <https://doi.org/10.1016/j.mattod.2019.11.003>.

References

- [1] P.M. Cox et al., *Nature* 408 (2000) 184.
- [2] W.R. Cline, *The Economics of Global Warming*, Institute for International Economics, Washington, 1992.
- [3] M. Meinshausen et al., *Nature* 458 (2009) 1158.
- [4] M.A. Green, A. Ho-Baillie, H.J. Snaith, *Nat. Photonics* 8 (2014) 506.
- [5] N.J. Jeon et al., *Nat. Mater.* 13 (2014) 897.
- [6] M. Liu, M.B. Johnston, H.J. Snaith, *Nature* 501 (2013) 395.
- [7] J. Burschka et al., *Nature* 499 (2013) 316.
- [8] Q. Chen, H. Zhou, Z. Hong, S. Luo, H.-S. Duan, H.-H. Wang, Y. Liu, G. Li, Y. Yang, *J. Am. Chem. Soc.* 136 (2014) 622–625.
- [9] G.E. Eperon et al., *Adv. Funct. Mater.* 24 (2014) 151–157.
- [10] D. Liu, T.L. Kelly, *Nat. Photonics* 8 (2013) 133.
- [11] H. Zhou et al., *Science* 345 (2014) 542–546.
- [12] W. Nie et al., *Science* 347 (2015) 522–525.
- [13] A. Mei et al., *Science* 345 (2014) 295–298.
- [14] S. Sanchez, X. Hua, N. Phung, U. Steiner, A. Abate, *Adv. Energy Mater.* 8 (2018) 1702915.
- [15] Q. Chen et al., *Sustainable Energy Fuels* 2 (2018) 1216–1224.
- [16] K. Hwang et al., *Adv. Mater.* 27 (2015) 1241–1247.
- [17] D. Vak et al., *Adv. Energy Mater.* 5 (2015) 1401539.
- [18] N.K. Noel et al., *Energy Environ. Sci.* 10 (2017) 145–152.
- [19] S. Sanchez, U. Steiner, X. Hua, *Chem. Mater.* 31 (2019) 3498–3506.
- [20] S. Sánchez et al., *Mater. Today* 31 (2019) 39–46, <https://doi.org/10.1016/j.mattod.2019.04.021>.
- [21] J.-A. Alberola-Borràs et al., *Science* 9 (2018) 542–551.
- [22] T. Homola et al., *ACS Appl. Mater. Interfaces* 8 (2016) 33562–33571.
- [23] T. Watson et al., *Prog. Photovoltaics Res. Appl.* 19 (2011) 482–486.
- [24] H.-E. Wang et al., *J. Phys. Chem. C* 115 (2011) 10419–10425.
- [25] A. Hadi et al., *Appl. Surf. Sci.* 428 (2018) 1089–1097.
- [26] S.-H. Turren-Cruz, A. Hagfeldt, M. Saliba, *Science* 362 (2018) 449–453.
- [27] Z. Li et al., *Chem. Mater.* 28 (2016) 284–292.
- [28] W.-G. Li et al., *J. Mater. Chem. A* 5 (2017) 19431–19438.
- [29] Z. Wang et al., *Nat. Energy* 2 (2017) 17135.
- [30] J.-W. Lee et al., *Adv. Energy Mater.* 5 (2015) 1501310.
- [31] D.J. Kubicki et al., *J. Am. Chem. Soc.* 140 (2018) 3345–3351.
- [32] X. Hou et al., *J. Mater. Chem. A* 5 (2017) 73–78.
- [33] G. Giorgi et al., *J. Phys. Chem. C* 119 (2015) 4694–4701.
- [34] L. Dimesso et al., *Mater. Sci. Eng., B* 204 (2016) 27–33.
- [35] A.D. Jodlowski et al., *Nat. Energy* 2 (2017) 972–979.
- [36] N.D. Pham et al., *Nano Energy* 41 (2017) 476–487.
- [37] N. De Marco et al., *Nano Lett.* 16 (2016) 1009–1016.
- [38] O.J. Weber et al., *Chem. Mater.* 30 (2018) 3768–3778.
- [39] P. Gratia et al., *ACS Energy Lett.* 2 (2017) 2686–2693.
- [40] L. Gu et al., *Nanoscale* 10 (2018) 15164–15172.
- [41] N.J. Jeon et al., *Nature* 517 (2015) 476.
- [42] C. Yi et al., *Energy Environ. Sci.* 9 (2016) 656–662.
- [43] G.E. Eperon et al., *Energy Environ. Sci.* 7 (2014) 982–988.
- [44] W.S. Yang et al., *Science* 356 (2017) 1376–1379.
- [45] G.P. Nagabhushana, R. Shivaramaiah, A. Navrotsky, *Proc. Natl. Acad. Sci. U.S.A.* 113 (2016) 7717.
- [46] K. Galkowski et al., *Energy Environ. Sci.* 9 (2016) 962–970.
- [47] A.A. Zhumekenov et al., *ACS Energy Lett.* 1 (2016) 32–37.
- [48] K. Madhusudan Reddy, S.V. Manorama, A. Ramachandra Reddy, *Mater. Chem. Phys.* 78 (2003) 239–245.
- [49] Y. Matsumoto et al., *Science* 291 (2001) 854–856.
- [50] R.I. Bickley et al., *J. Solid State Chem.* 92 (1991) 178–190.
- [51] Q. Han et al., *Adv. Mater.* 28 (2016) 2253–2258.
- [52] W. Rehman et al., *Adv. Mater.* 27 (2015) 7938–7944.
- [53] O. Nazarenko et al., *NPG Asia Mater.* 9 (2017) e373.
- [54] Y. Hu et al., *ACS Energy Lett.* 2 (2017) 2212–2218.
- [55] Q.A. Akkerman et al., *J. Am. Chem. Soc.* 137 (2015) 10276–10281.
- [56] T. Meier et al., *J. Mater. Chem. C* 6 (2018) 7512–7519.
- [57] C. Roldán-Carmona et al., *Energy Environ. Sci.* 8 (2015) 3550–3556.
- [58] F. Liu et al., *Adv. Energy Mater.* 6 (2016) 1502206.
- [59] S. Sanchez et al., *Adv. Energy Mater.* 8 (2018) 1802060.
- [60] W. Li et al., *Nat. Rev. Mater.* 2 (2017) 16099.
- [61] P. Wang et al., *J. Phys. Chem. Lett.* 8 (2017) 2119–2125.
- [62] V. D’Innocenzo et al., *J. Am. Chem. Soc.* 136 (2014) 17730–17733.
- [63] F. Hao et al., *Nat. Photonics* 8 (2014) 489.
- [64] D.P. McMeehan et al., *Science* 351 (2016) 151–155.
- [65] W. Tress et al., *Nat. Energy* 4 (2019) 568–574.
- [66] K. Domanski et al., *Nat. Energy* 3 (2018) 61–67.
- [67] K. Domanski et al., *Energy Environ. Sci.* 10 (2017) 604–613.
- [68] M. Saliba et al., *Energy Environ. Sci.* 9 (2016) 1989–1997.
- [69] H.J. Snaith et al., *J. Phys. Chem. Lett.* 5 (2014) 1511–1515.
- [70] J.M. Ball et al., *Energy Environ. Sci.* 6 (2013) 1739–1743.